Rhesus Monkey Brain Imaging Through Intact Skull with Thermoacoustic Tomography

Yuan Xu and Lihong V. Wang, *Senior Member, IEEE*

Abstract—Two-dimensional microwave-induced thermoacoustic tomography (TAT) is applied to imaging the Rhesus monkey brain through the intact skull. To reduce the wavefront distortion caused by the skull, only the low-frequency components of the thermoacoustic signals (< 1 MHz) are used to reconstruct the TAT images. The methods of signal processing and image reconstruction are validated by imaging a lamb kidney. The resolution of the system is found to be 4 mm when we image a 1-month-old monkey head containing inserted needles. We also image the coronal and axial sections of a 7-month-old monkey head. Brain features that are 3 cm deep in the head are imaged clearly. Our results demonstrate that TAT has potential for use in portable, cost-effective imagers for pediatric brains.

I. Introduction

THERMOACOUSTIC tomography (TAT) is a novel, noninvasive, and nonionizing imaging modality [1]–[8]. In TAT, a microwave or laser pulse is used to irradiate the tissues. When the electromagnetic radiation is absorbed by the biological tissues, the heating and subsequent expansion causes the emission of acoustic waves, which is called the thermoacoustic effect. The thermoacoustic signals are collected to map the distribution of radiative absorption within the tissues, which is closely related to the physiological and pathological status of the tissues [9]–[12]. The TAT combines the good contrast of the optical or electromagnetic imaging modalities with the high resolution of the ultrasound imaging modalities. Besides structural imaging, TAT has been applied to the functional imaging of blood [13] when a laser is used.

Current high-resolution human brain imaging modalities include X-ray computerized tomography (CT), magnetic resonance imaging (MRI), and sonography. However, both CT and MRI are expensive, and neither is portable. Furthermore, X-ray CT uses ionizing radiation. The development of an affordable, nonionizing, high-resolution imaging modality that can be used in operating rooms or at the bedside to monitor brain conditions such as strokes, head injuries, tumors, and brain infections, therefore, is highly desirable. In certain cases, ultrasound brain imaging comes close to meeting these objectives. For example, ultrasound imaging is an established pediatric brain imaging modality when used before the fontanelles are closed. After the closure of the fontanelles, the image quality degrades significantly because the skull severely attenuates and scatters ultrasonic waves. The skull consists primarily of three layers: the outer and the inner ivory tables and the dipole. The ivory tables cause attenuation primarily through reflection at the interfaces, and the dipole can induce both strong attenuation and scattering, both of which increase rapidly with frequency. Nevertheless, in the frequency range below 1 MHz, the distortion and attenuation of the human skull is shown to be minimal [14]. Fry *et al.* [15] reported on an ultrasonic diagnostic system for interactive interrogation of the adult brain through an intact skull; their system used 0.75 MHz ultrasound in the B-mode and was able to image some internal structures of the human brain. Other reported methods using ultrasound for brain imaging include computed ultrasound attenuation tomography [16] and ultrasonic reflection mode computed tomography [17]. However, with these methods, the resolution is poor in the obtained images, and only a few structures can be identified.

In this paper, we present our results on monkey brain imaging with two-dimensional (2-D) microwave-induced TAT, which represents a first step toward human brain TAT. Compared with pure ultrasound brain imaging, brain TAT has the advantages of good contrast and less skull distortion, as will be shown in Section III. Although rat brain imaging with laser-induced TAT has been previously studied [13], to the best of our knowledge, no results on applying TAT to primate brain imaging have been published. In rat brain imaging, the effects of the rat skull can be ignored because the rat skull is less than 1 mm thick. In our experiments, we use 3 GHz microwaves, which are able to penetrate several centimeters into tissue. Therefore, our system has potential for deep human brain imaging, especially in infants. In Section II, the experimental setup, the methods for signal processing and image reconstruction, and sample preparation are introduced. In Section III, we first show the results of imaging a lamb kidney. Then, we present some TAT images of monkey heads. We also discuss the heating effect of microwave and safety issue, and recommend some potential improvements for future studies.

II. Methods

A. Experimental Setup

The experimental setup for this study is shown in Fig. 1. A Cartesian coordinate system is set up for reference: the x

Fig. 1. Diagram of the experimental setup.

Fig. 2. Average temporal spectral intensity of the thermoacoustic signals corresponding to Fig. 3.

Fig. 3. (a) 2-D thermoacoustic image of an excised whole lamb kidney. (b) Corresponding photograph of the opened kidney after being fixed by formalin.
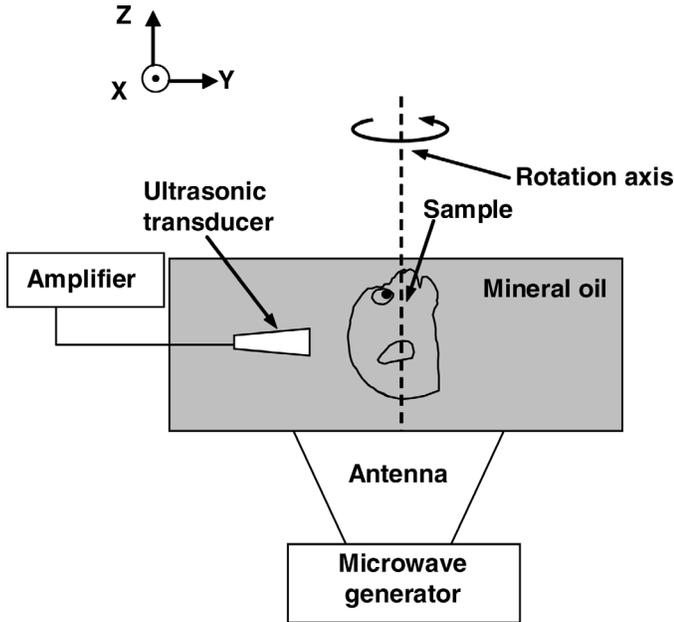
axis points outward perpendicularly to the drawing plane; the y axis points to the right; and the z axis points upward along the rotation axis. A 3-GHz microwave generator transmits 0.5 μs microwave pulses at a repetition rate of 20 Hz. A function generator is used to trigger the microwave generator, control its pulse repetition frequency, and synchronize the sampling by the oscilloscope. Microwave energy ($\sim$10 mJ/pulse) is delivered by an antenna with a cross section that gradually changes from 72 mm × 34 mm to 120 mm × 88 mm. Therefore, the flux is on the order of 0.1 mJ/cm^2 at the exit of the antenna.

We used two types of ultrasonic transducers. The central frequency of the ultrasonic transducers is 1 MHz; the bandwidth is about 0.8 MHz. The first one is a cylindrically focused ultrasonic transducer with an active-element aperture of 2.5 cm and 0.6 cm along the z axis and the x-y plane, respectively. The transducer is curved along the z direction and has a focal length of 7.5 cm. The second one is a flat transducer with a circular surface with an active-element aperture of 6 mm in diameter. When the focused transducer is used, the center of the object is put at the focus of the transducer. When the flat transducer is used, the distance between the object's center and the detector is within the range of 8–14 cm in our experiments. Therefore, the sample is located in the far field of the transducer. The receiving directivity of the circular flat transducer can be expressed as $S(\theta) = J_1(u)/u$, where $u = 2\pi a\theta/\lambda$, a is the radius of the transducer element, λ is the acoustic wavelength, and θ is the direction relative to the acoustic axis. The angular spread is $\theta_0 = 0.61\lambda/a$. For $a = 3$ mm, and $\lambda = 3$ mm, the angular spread is about 34 degrees. If the distance between the head and the detector is about 8 cm, the resolution of the flat transducer along the z direction is about 11.2 cm. The low resolution along the z direction can cause artifacts in the 2-D TAT because the structures
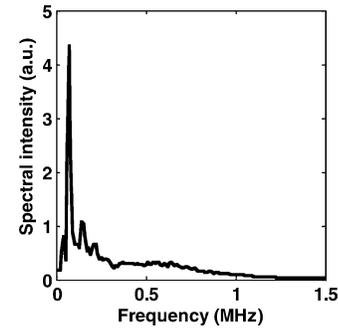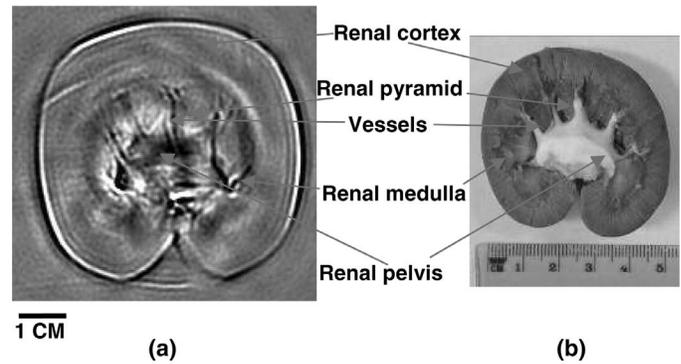
around the imaging plane can be superposed to the image section.

The to-be-imaged monkey head, which is immersed in mineral oil, is held in place by a clamp that is mounted on a rotary table in the x-y plain; the table is driven by a computer-controlled stepper motor. The transducer is connected to a pulse amplifier, and the amplified signal is averaged 400 times and recorded by an oscilloscope before being transferred to a personal computer. During the experiment, the transducer scans around the sample through 160 steps with a step size of 2.25 degrees. The total data acquisition time is about 80 minutes. At each step, the thermoacoustic signals are sampled for 100 μs at a sampling rate of 20 MHz. The scanning radius is within the range of 6–14 cm in our experiments. More details on the experimental setup can be found in our group's previous paper [5].

B. Reconstruction Method and Signal Processing

A backprojection algorithm is used in our reconstruction [5]. However, the raw data is processed before the reconstruction. First, a low-pass filter is applied to filter out the frequency components above 1 MHz, because the high-frequency component is expected to be strongly distorted by the skull. Second, a high-pass filter designed by the method introduced in [18] is used to reduce the low-
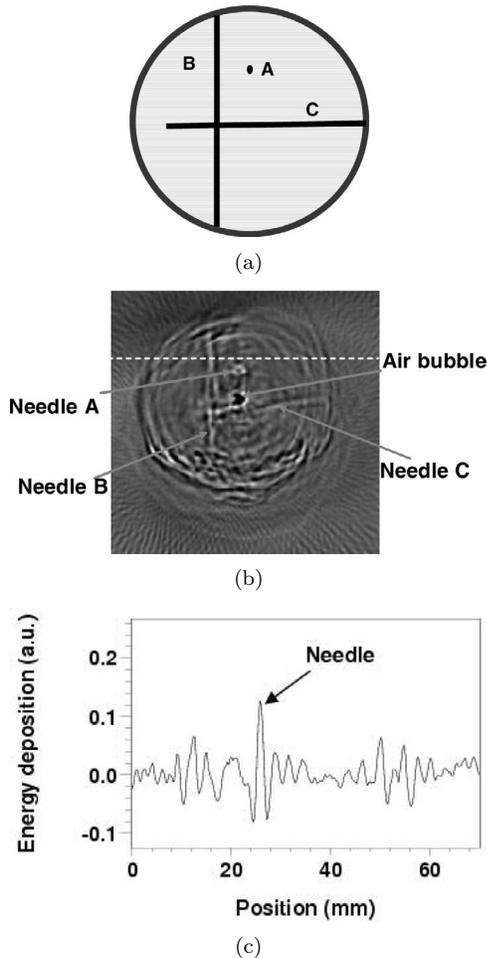
(a)

(b)

(c)

Fig. 4. (a) Diagram showing a monkey head with three inserted needles. (b) TAT image. (c) The line plot along the dashed line in (b).

frequency components to achieve the best spatial resolution. An example of the spectral shape of the final filter is shown in [18]. Fig. 2 shows the average spectral intensity of the TAT data corresponding to Fig. 3. The TAT signal is predominated by the components with frequencies of less than 0.2 MHz. One reason for this spectral profile is the heterogeneity of the microwaves. The wavelength of a microwave at 3 GHz in tissues is on the order of 1.5 cm. This can induce a periodic spatial distribution of microwave absorption in the tissue. Consequently, we observe strong frequency components in the thermoacoustic signals at about 0.1 MHz. If the thermoacoustic signals are not processed before the reconstruction, the reconstructed images will look blurred because the resolution of TAT is inversely proportional to the bandwidth of the thermoacoustic signals. To improve image resolution, we divide the spectral intensity of the thermoacoustic signals by their average spectral amplitude (Fig. 2) in order to reduce the amplitude of the low-frequency components and, consequently, increase the bandwidth of the thermoacoustic signals. This signal processing technique has been tested in [18] by a numerical simulation as well as experimental results. To verify our methods of signal processing and image reconstruction, we image an excised lamb kidney (Fig. 3).

The TAT images are the results of the spatial band-pass filtering of the distribution of the energy deposition in the sample. Therefore, it has both positive and negative values. The point spread function or the transfer function of the spatial band-pass filtering $S(R)$ is related to the temporal transfer function of the detection system as $T(\omega)$ as $S(R) = (1/2\pi^2) \int_0^{+\infty} T(\omega) j_0(\omega R) \omega^2 d\omega$, where R is the distance in the image between a point and the position of the point object. $T(\omega)$ includes two parts. The first part is the receiving spectrum of the detector. The second part is introduced in the signal processing as shown above. Both of them are usually in the form of a bandpass filter.

C. Sample Preparation

The head samples were dissected and stored in formalin or mineral oil. We found that the brain tissue still looked fresh when the skull was opened, even after the heads had been immersed in formalin with intact skull for 2 weeks. This is because it is hard for formalin to penetrate the skull. The long hair on the heads was cut off to reduce the potential attenuation to acoustic waves.

III. RESULTS AND DISCUSSION

A. Experimental Results

The photograph and the TAT image of the excised lamb kidney are shown in Fig. 3. The kidney is put in a small container, which makes it look more round than its natural shape. The TAT image agrees well with the photograph of the kidney sliced after the TAT data acquisition. The center of the kidney is the renal pelvis, which is white in the photograph and appears dark in the TAT image. In the photograph, the white branches from the renal pelvis are blood vessels, which are shown clearly in the TAT image. It should be noted that, in the photograph of the kidney, each branch from the pelvis contains several blood vessels, and the different vessels in some branches can be distinguished clearly in the TAT image. Some small vessels between branches also are imaged correctly.

Rhesus monkey heads are used next in our experiments. We first investigated the effects of the skull on 2-D TAT with a cylindrically focused ultrasonic transducer. Then, we imaged the coronal and axial sections of a monkey head using an unfocused ultrasonic transducer. We will explain below whether or not a focused transducer should be used.

In the first experiment, a 1-month-old monkey with a skull thickness of less than 1 mm was used. The size of the coronal cross section of the head in the imaging plane is 53 mm by 51 mm. We inserted three needles (0.9 mm diameter) into the head: these are perpendicular to each other [Fig. 4(a)]. Two of them are in the x-y plane (the imaging plane). The needles are used because they have good contrast in soft tissue and can be used to estimate the image resolution in the x-y plane. To improve the resolution along the z-direction, we used a cylindrically focused ultrasonic
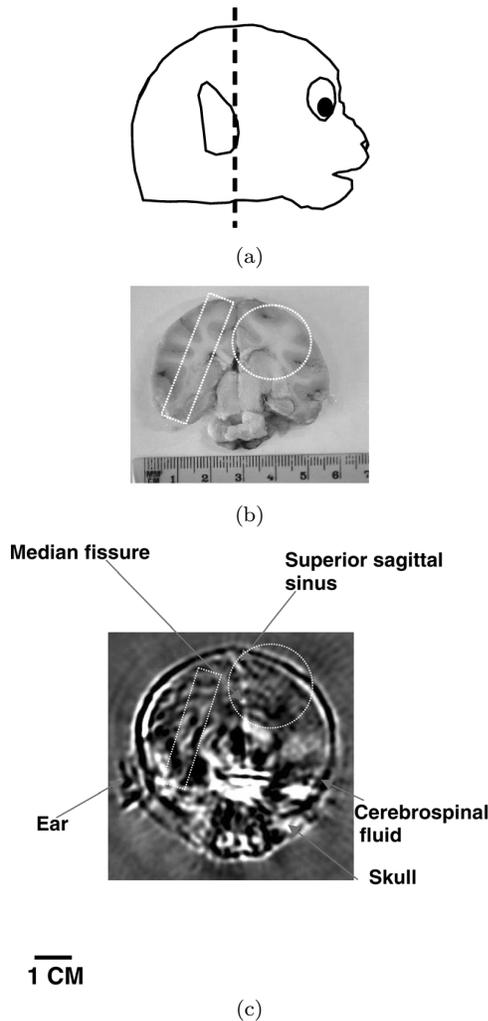
Fig. 5. (a) Diagram showing the coronal imaging plane. (b) The photograph of the imaged cross section. (c) The corresponding TAT image. Note some similar features between the TAT image and the photograph, such as the star-shaped white matter (dotted circle in the TAT image and photograph) and a long stripe of white matter from the left top to the left bottom (dotted rectangular).

transducer, which is 2.5 cm and 6 mm along the z axis and the x-y plane, respectively. The transducer is curved along the z direction and has a focal length of 7.5 cm. The transducer scans around the sample along a circle with a radius of about 8 cm. Fig. 4(b) is the TAT image, which shows the three needles clearly. Fig. 4(c) is the line plot along the dashed line in Fig. 4(b). The resolution of the system is estimated to be about 4 mm, which is the width [defined as the distance between the two minima around the maxima in the line plot Fig. 4(c)] of the needles in this image. The black spot at the center of the image is probably an air bubble introduced when inserting the needles. This image shows that brain TAT can survive the distortion caused by the skull if there is enough contrast or signal-to-noise-ratio (SNR). However, we cannot identify any internal brain structures in this image. It is probably because the signals from the needles are much stronger than the signals from the internal structures. Another problem in the image is that the boundary of the head is not clear compared

with Fig. 5(c). This is because the boundary of the head is out of the focal zone of the transducer; therefore, the signals from a point at the boundary will reach different parts of the curved transducer at different times. However, in the reconstruction, the transducer is treated as a point detector. Therefore, after backprojection, the signals arriving at different times will yield multiple boundaries. Based on this result, we decided to use a flat transducer (with a diameter of 6 mm) in our later experiments.

In the next experiments, we imaged the brain of a 7-month-old Rhesus monkey through the intact skull (skull thickness, 1–2 mm). The transducer scans along a circle with a radius of 14 cm. Fig. 5(a) shows the side view of the monkey head, and the dashed line shows approximately the imaging plane. We choose this plane because the skull at the boundary is perpendicular to the imaging plane. Otherwise, the acoustic waves will be attenuated and scattered strongly when the ultrasonic waves propagate obliquely to the skull [16]. Fig. 5(b) is a photograph of the brain slice around the imaging plane from another monkey head, and Fig. 5(c) is the TAT image. During the dissection, the cerebellum was damaged because it had not been fixed well. Consequently, only the cerebra and the middle brain are shown in the photograph, which makes the brain in the photograph look smaller than in the TAT image. In the TAT image, the grey matter and cerebrospinal fluid (CSF) appear darker (more water), and the white matter appears whiter (less water). The most easily identified structure in the TAT image is the white middle line, which is the median fissure, the gap between the left and right cerebral hemispheres. At the top of the middle line, the straight line turns to the left side; this represents the superior sagittal sinus (SSS). At the bottom of the central vertical line, there is a horizontal line, which is the space between the middle brain and cerebellum. However, the white matter in the TAT image does not exactly match the white matter on the photograph. Nevertheless, we can see some similar branch patterns and features between them, such as the star-shaped white matter (dotted circle in the TAT image and photograph) and the long stripe of white matter from the top left to the bottom left (dotted rectangular). It should be noted that the resolution along the z axis in the 2-D TAT is quite limited; therefore, the structures around the image plane might be superposed onto the image. This makes some structures in the TAT image hard to identify. We will discuss this issue in more detail in Section III-B.

Fig. 6(a) shows the TAT image in another coronal imaging plane [Fig. 6(c)], which is behind the previous one. Fig. 6(b) is the corresponding photograph of the slice around the imaging plane. The branch structure of the white matter is imaged. The median fissure and the boundary between the cerebra and cerebella also are imaged. There seem to be more artifacts in Fig. 6 than Fig. 5, which may be explained by the fact that the skull is somewhat oblique to the imaging plane in this case.

Fig. 7(b) shows the TAT image of an axial cross section [Fig. 7(a)], which is chosen to be perpendicular to the skull
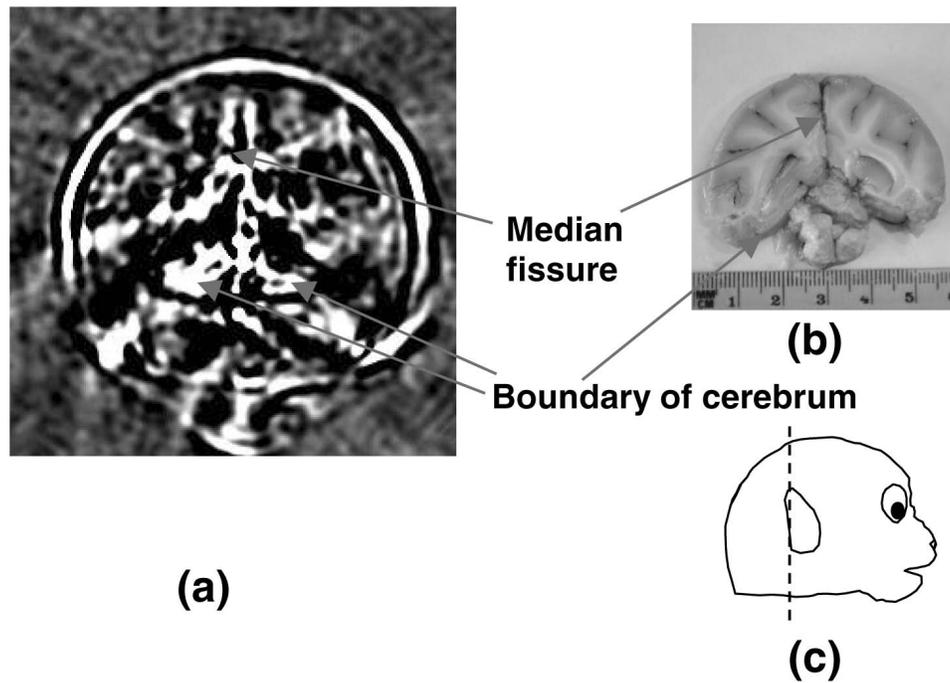
Fig. 6. (a) TAT image of another coronal cross section of the head. (b) The corresponding photograph. (c) Diagram showing the coronal imaging plane.

in the same plane. The white structures in Fig. 7(b) have less water content than the black ones. Many features of the TAT image are symmetrical with respect to the middle vertical line, which agrees with the brain anatomy. The most obvious structure is the corpus callosum, which is the low-water-content fiber connecting the two cerebral hemispheres.

B. Discussion

1. Advantages of TAT: Compared with pure ultrasound brain imaging, it is expected that there will be less distortion caused by the skull with TAT because in TAT the acoustic source is induced by electromagnetic absorption; therefore, only one-way distortion on the reception wave propagation occurs. By contrast, in ultrasound tomography (UT), either in the pulse-echo mode or in the transmission mode, ultrasound distortion includes two parts because distortion arises during both the transmission and the reception wave propagation. Unlike ultrasonic time-of-flight tomography and attenuation tomography, 2-D TAT has the potential for real-time brain imaging when an ultrasound array is used.

2. Potential Improvement: Although our preliminary results on brain TAT are encouraging, there is still room for significant improvement. The first such improvement would be to use 3-D TAT. TAT is intrinsically a 3-D imaging modality. It is necessary to collect the TAT signal from a 2-D detection surface to achieve a complete reconstruction. The 2-D TAT used in our experiments can obtain only an approximate image of the sample's cross section in the imaging plane. There are two kinds of errors in 2-D TAT. The first kind of error occurs when the objects around the

imaging plane are projected onto the imaging plane. This is because the transducer is flat and has a diameter of 6 mm. Therefore, the resolution along the z direction (perpendicular to the imaging plane) is quite limited (worse than 6 mm). However, with objects within the imaging plane, if its boundary is more or less oblique to the imaging plane, the TAT signals from these boundaries will be missed. According to our study on the limited-view TAT [19], these boundaries will not be reconstructed sharply in the 2-D TAT. These errors in 2-D TAT are the important factor that causes the discrepancy between our TAT images in Figs. 5 and 6, and the corresponding photograph. Therefore, it is expected that 3-D TAT will improve the image quality significantly.

Other electromagnetic waves besides microwaves also can be applied to brain TAT. For example, (near) infrared light can penetrate tissues several centimeters. Unlike microwave, there is no centimeter-scale periodic heterogeneity in infrared laser illumination. Therefore, the low-frequency disturbance can be reduced significantly. Another advantage of using a (near) infrared laser is that the SNR can be increased greatly by a significant increase of the illumination energy given the same illumination area. For example, in our experiments, the energy of a single microwave pulse is about 10 mJ, and it is easy to find a commercial laser providing a single pulse energy of about several hundred millijoule. In addition, laser-induced TAT can provide more functional information than microwave TAT. Another potential improvement of TAT brain imaging is to apply aberration correction techniques to reduce the artifacts induced by the skull [20]–[22].

In our preliminary experiments, the monkey heads were immersed in mineral oil. However, when an ultrasound ar-

(a)

Median fissure

Cerebrospinal fluid

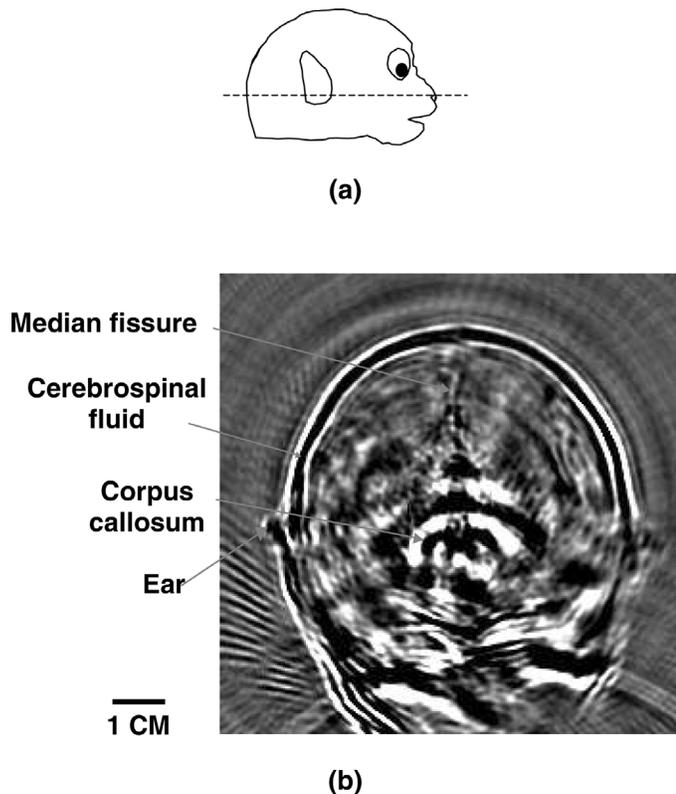Corpus callosum

Ear

1 CM

(b)

Fig. 7. (a) Diagram showing the axial imaging plane. (b) TAT image. The top of (b) represents the rear part of the head.

ray becomes available, ultrasound gel coupling can be used instead, which is more suitable for in vivo investigations. In some clinical applications, it might be difficult to couple a full 2π circular array to the head. Nevertheless, our previous study shows that a limited-view detection still can yield a complete reconstruction [19].

3. Heating Effect and Microwave Safety Issue: The temperature rise ΔT in the tissue caused by each microwave pulse can be estimated as:

$$\Delta T = \frac{\alpha P \tau}{S \rho C},\tag{1}$$

where α is microwave energy absorption rate of the high-water-content tissue (~ 1 cm^{-1}), C is the specific heat of the tissue, ρ is the density of the tissue, P is the average power in each microwave pulse, τ is the microwave pulse width, and S is the area of the attenna exit. Substituting the experimental parameters in Section II, we have $\Delta T = 2 \times 10^{-5}$ degree for a single microwave pulse. Considering that we have 160 scanning steps and 400 times averaging at each step, we have the total temperature rise of 1.3 degree after the data acquisition for a TAT image, even if there is no heat conduction to dissipate the heat at all. This small heating effect should be safe for clinical applications.

According to the IEEE standard [23], our case involves microwave exposures under a controlled environment, which means that exposure is incurred by persons who are aware of the potential of exposure. For the 3-

GHz microwave under a controlled environment, the upper limit of safe exposure is 10 mW/cm^2. If it is used for partial-body exposure, according to the relaxation of power density limits, the upper limit is 20 mW/cm^2 for 3-GHz microwaves. Additionally, for exposures to pulsed radio frequency fields, if there are no more than five pulses in the 6 minutes averaging time and the pulse duration is less than 100 ms, the power density of the pulsed microwaves should be multiplied by five to compare with the normal upper limit. In our situation, there are more than five pulses during the 6 minutes averaging time, so the power density of pulsed microwaves should compare directly with the normal upper limits.

The nominal peak power of our 3-GHz microwave generator is 20 kW; the microwave pulse width is 0.5 μs; the pulse repetition rate is about 20 Hz; and the outlet of the microwave antenna is 120 mm $\times$ 88 mm. Therefore, the power density of the 3-GHz microwave system is 1.9 mW/cm^2, which is within the IEEE safety standard—20 mW/cm^2.

We have assumed in these calculations that the entire microwave has been coupled out of the antenna without divergence. In the experiments, however, only part of the microwave is coupled out of the antenna and further diverged into a much larger area than the outlet of the antenna. The power densities used in our experiments are below the limits of the IEEE standard and should be safe when applied to humans.

IV. Conclusions

We first investigated the effect of the skull on 2-D TAT, which is the primary factor hindering conventional ultrasound imaging of the brain. We found that thermoacoustic signals still can be detected by our system, even after being attenuated by the skull. This is because the acoustic signals induced in microwave TAT are low-frequency pulses (~ 1 MHz), which can penetrate the skull with minimal distortion. Then, we imaged the coronal and axial sections of monkey heads using both cylindrically focused and unfocused ultrasonic transducers. Brain features that are 3 cm deep in the head were imaged clearly. The resolution of the system was found to be 4 mm when imaging a 1-month-old monkey head containing three needles. 3-D TAT and a more homogeneous electromagnetic illumination with higher energy are expected to further improve the imaging quality.

Acknowledgments

REFERENCES

[1] T. Bowen, "Radiation induced thermoacoustic imaging," U.S. Patent # 4,385,634, May 31, 1983.
[2] T. Bowen, "Radiation-induced thermoacoustic soft tissue imaging," in *Proc. IEEE Ultrason. Symp.*, 1981, pp. 817–822.
[3] T. Bowen, R. L. Nasoni, A. E. Pifer, and G. H. Sembroski, "Some experimental results on the thermoacoustic imaging of tissue equivalent phantom materials," in *Proc. IEEE Ultrason. Symp.*, 1981, pp. 823–827.
[4] Y. Xu, D. Feng, and L.-H. V. Wang, "Exact frequency-domain reconstruction for thermoacoustic tomography: I. Planar geometry," *IEEE Trans. Med. Imag.*, vol. 21, pp. 823–828, 2002.
[5] M. Xu and L.-H. V. Wang, "Time-domain reconstruction for thermoacoustic tomography in a spherical geometry," *IEEE Trans. Med. Imag.*, vol. 21, pp. 814–822, 2002.
[6] Y. Xu, M. Xu, and L.-H. V. Wang, "Exact frequency-domain reconstruction for thermoacoustic tomography: II. Cylindrical geometry," *IEEE Trans. Med. Imag.*, vol. 21, pp. 829–833, 2002.
[7] R. A. Kruger, P. Liu, Y. R. Fang, and C. R. Appledorn, "Photoacoustic ultrasound (PAUS)-reconstruction tomography," *Med. Phys.*, vol. 22, pp. 1605–1609, 1995.
[8] C. G. A. Hoelen, F. F. M. Mul, R. Pongers, and A. Dekker, "Three-dimensional photoacoustic imaging of blood vessels in tissue," *Opt. Lett.*, vol. 23, pp. 648–650, 1998.
[9] W. Joines, R. Jirtle, M. Rafal, and D. Schaeffer, "Microwave power absorption differences between normal and malignant tissue," *Radiation Oncol. Biol. Phys.*, vol. 6, pp. 681–687, 1980.
[10] S. Chaudhary, R. Mishra, A. Swarup, and J. Thomas, "Dielectric properties of normal human breast tissues at radiowave and microwave frequencies," *Indian J. Biochem. Biophys.*, vol. 21, pp. 76–79, 1984.
[11] W. Joines, Y. Zhang, C. Li, and R. Jirtle, "The measured electrical properties of normal and malignant human tissues from 50–900 MHz," *Med. Phys.*, vol. 21, pp. 547–550, 1994.
[12] W. F. Cheong, S. A. Prahl, and A. J. Welch, "A review of the optical properties of biological tissues," *IEEE J. Quantum Electron.*, vol. 26, pp. 2166–2185, 1990.
[13] X. Wang, Y. Pang, G. Ku, X. Xie, G. Stoica, and L.-H. Wang, "Non-invasive laser-induced photoacoustic tomography for structural and functional imaging of the brain in vivo," *Nature Biotech.*, vol. 21, pp. 803–806, 2003.
[14] F. Fry and J. Barger, "Acoustical properties of the human skull," *J. Acoust. Soc. Amer.*, vol. 63, pp. 1576–1590, 1978.
[15] F. Fry, N. Sanghvi, R. Morris, J. Clendenon, K. Dines, J. Patrick, and S. Goss, "Ultrasonic diagnostic system for interactive interrogation of adult brain through intact skull," *Invest. Radiol.*, vol. 17, pp. 463–469, 1982.
[16] K. Dines, F. Fry, J. Patrick, and R. Gilmor, "Computerized ultrasound tomography of the human head: Experimental results," *Ultrason. Imag.*, vol. 3, pp. 342–351, 1981.
[17] J. Ylitalo, J. Koivukangas, and J. Oksman, "Ultrasonic reflection mode computed tomography through a skullbone," *IEEE Trans. Biomed. Eng.*, vol. 37, pp. 1059–1066, 1990.
[18] Y. Xu and L.-H. Wang, "Signal processing in scanning thermoacoustic tomography in biological tissues," *Med. Phys.*, vol. 28, pp. 1519–1524, 2001.
[19] Y. Xu, L.-H. V. Wang, G. Ambartsoumian, and P. Kuchment, "Reconstructions in limited-view thermoacoustic tomography," *Med. Phys.*, vol. 31, pp. 724–733, 2004.
[20] M. Fink, G. Montaldo, and M. Tanter, "Time-reversal acoustics in biomedical engineering," *Ann. Rev. Biomed. Eng.*, vol. 5, pp. 465–497, 2003.
[21] S. W. Flax and M. O'Donnell, "Phase aberration correction using signals from point reflectors and diffuse scatters: Basic principles," *IEEE Trans. Ultrason., Ferroelect., Freq. Contr.*, vol. 35, pp. 758–767, 1988.
[22] G. E. Trahey, D. Zhao, J. A. Miglin, and S. W. Smith, "Experimental results with a real-time adaptive ultrasonic imagining system for viewing through distorting media," *IEEE Trans. Ultrason., Ferroelect., Freq. Contr.*, vol. 37, pp. 418–427, 1990.
[23] *IEEE Standard for Safety Levels with Respect to Human Exposure to Radio Frequency Electromagnetic Fields 3 kHz to 300 GHz, IEEE Standard C95.1*, 1999.